Atmospheric Research 346 (2027) 109439

Contents lists available at ScienceDirect

Atmospheric Research

journal homepage: www.elsevier.com/locate/atmosres

Research Paper

# Regime-dependent transmission of Tibetan Plateau intraseasonal oscillations modulates South China extreme rainfall

Meirong Wang [a,*], Xuepeng Cui [a], Shunwu Zhou [a,*], Jun Wang [b,d,e], Zhu Zhu [c], Cong Miao [a]

[a] State Key Laboratory of Climate System Prediction and Risk Management, Key Laboratory of Meteorological Disaster, Ministry of Education, Collaborative Innovation Center on Forecast and Evaluation of Meteorological Disasters, Nanjing University of Information Science and Technology, Nanjing, China
[b] International Institute for Earth System Science, Nanjing University, Nanjing, China
[c] College of Meteorology and Oceanography, National University of Defense Technology, Changsha, China
[d] Xizang Mèdog Field Scientific Observation and Research Station for Atmospheric Water Cycle, Mèdog, China
[e] Xigazè National Climate Observatory, CMA, Xigazè, China

ARTICLE INFO

*Keywords:*
Tibetan Plateau
Quasi-biweekly oscillation intensity
South China extreme precipitation
Baroclinic energy conversion
Subseasonal-to-seasonal prediction

ABSTRACT

Unraveling the trans-regional drivers of early-summer extreme precipitation over South China is crucial for bridging the subseasonal-to-seasonal (S2S) predictability gap. A regime-dependent teleconnection is demonstrated between the interannual variability of June Tibetan Plateau (TP) quasi-biweekly oscillation intensity (QBWOI) and South China extreme rainfall, with upstream atmospheric heat source precursors lead downstream hydrological hazards by approximately 8 days. A robust negative correlation is identified, driven by asymmetric subseasonal propagation pathways and downstream energetic-dynamic gating mechanisms. During strong TP QBWOI years, perturbations along the TP's southeastern flank steer downstream, triggering negative baroclinic energy conversion ($CP < 0$) that suppresses localized eddy growth over South China. This modulation is achieved by a northwestward-shifted South Asian High (SAH) and an eastward-retreated Western Pacific Subtropical High (WPSH), which jointly produce deep subsidence and moisture divergence. Conversely, weak years activate an alternative zonal eastward pathway from the TP interior into a positive baroclinic energy conversion hotbed ($CP > 0$). Coordinated by an eastward-extended SAH and a westward-advanced WPSH, an anomalous low-level cyclonic pump channels abundant tropical moisture to drive vigorous upward motion, thereby fostering widespread extreme rainfall. Overall, these findings highlight that the TP QBWO background serves as an important prognostic indicator for improving S2S predictive skill for East Asian hydrological extremes.

## 1. Introduction

Under global warming, the frequency, intensity, and duration of extreme precipitation events exhibit distinct upward trends globally and regionally (e.g., Myhre et al., 2019; Jin et al., 2025; Khadke et al., 2026). As a densely populated and economically vibrant hub, South China is exceptionally vulnerable to such climatic shifts due to the intense overlap between high hazard exposure and dense socioeconomic infrastructure. Extreme precipitation during its pre-flood season—particularly in June—frequently triggers severe and abrupt drought-flood transitions (Gu et al., 2018; Feng et al., 2025). This period coincides with the full onset and northward advancement of the East Asian summer monsoon, making the regional hydrological cycle highly sensitive to multi-scale atmospheric perturbations. Consequently, deciphering the multi-scale drivers of regional precipitation during this period is a critical cornerstone for narrowing the predictability gap within the subseasonal-to-seasonal (S2S) forecasting window (Vitart and Robertson, 2018; Luo et al., 2020; Xie et al., 2023).

From a multi-scale perspective, precipitation during the South China pre-flood season is modulated by an intricate interplay of drivers across varying timescales. Previous studies have demonstrated that external forcing anomalies and large-scale circulation systems—such as sea surface temperature (SST) anomalies (Yang et al., 2023), the thermal status of the Tibetan Plateau (Kong et al., 2025; Li et al., 2025), and the Western Pacific Subtropical High (Fang et al., 2023)—establish the favorable background environmental fields on seasonal-to-interannual timescales. Nonetheless, the intraseasonal variability constitutes a prominent component of South China rainfall dynamics. Accumulating

* Corresponding authors.
*E-mail addresses:* wmr@nuist.edu.cn (M. Wang), zhou@nuist.edu.cn (S. Zhou).

https://doi.org/10.1016/j.atmosres.2026.109439
Received 22 August 2026; Received in revised form 19 October 2026; Accepted 5 November 2026
Available online 7 November 2026
0169-8095/© 2026 Elsevier B.V. All rights are reserved, including those for text and data mining, AI training, and similar technologies.

evidence indicates that both tropical intraseasonal signals, such as the 10–30-day Boreal Summer Intraseasonal Oscillation (BSISO) (Hsu et al., 2016; Ren et al., 2018; Liu and Lu, 2022) and 30–60-day oscillations (Zang et al., 2024), and mid-latitude waves heavily modulate regional convection systems (Pan et al., 2025; Yan et al., 2025). Crucially, among these intraseasonal modes, the 10–20-day low-frequency oscillation exerts a substantially stronger contribution to persistent heavy rainfall events and total precipitation volume over South China (e.g., Hong et al., 2021; Qiu et al., 2022; Li et al., 2024; Yan et al., 2025; Lu et al., 2026).

As a core active center for mid-latitude ISOs, the Tibetan Plateau (TP) exhibits pronounced quasi-biweekly oscillation (QBWO, 10–20-day) signals across various meteorological fields (Wang and Duan, 2015; Yuan et al., 2023; Guo et al., 2024; Wang et al., 2026), which profoundly shape regional and downstream climate anomalies (Yang et al., 2017; Hu et al., 2023; Xie et al., 2026), and alter the progression of the East Asian summer monsoon (Fujinami and Yasunari, 2009). These upstream low-frequency perturbations propagate downstream along a distinct pathway, preceding downstream precipitation variations by approximately 2–8 days (Wang et al., 2019). However, while previous studies have heavily focused on the climatological mean features of this downstream propagation, the amplitude, structure, and propagation pathways of the TP QBWO display prominent interannual heterogeneity, which constrains the severity of regional extreme rainfall and limits its subseasonal predictability (Zhang et al., 2024; Guo et al., 2025; Zhu et al., 2025, 2026). This interannual fluctuation in TP QBWO intensity (QBWOI) profoundly shapes downstream drought and flood conditions. Concurrently, mid-to-high latitude low-frequency signals propagate southeastward as Rossby wave trains to impact South China (Miao et al., 2019; Zeng and Sun, 2023), with the TP serving as an indispensable geographical and dynamical conduit (Fujinami and Yasunari, 2009; Li and Mao, 2019). Crucially, whether these downstream-propagating waves are channeled via a northern circumglobal waveguide or steered along a southern subtropical track remains highly variable on interannual timescales (Miao et al., 2019; Ding and Wang, 2005).

Despite these insights, how the interannual variability of early-summer TP QBWOI regulates subseasonal transmission pathways and dynamic environments governing South China's pre-flood extreme precipitation remains unresolved. Given that subseasonal guiding environments—such as the Western Pacific Subtropical High (WPSH) and upper-level the jet stream—undergo pronounced interannual realignments, we hypothesize that the downstream transmission of the TP QBWO follows regime-dependent pathways under varying background-flow conditions. Specifically, the precise dynamic mechanisms through which these upstream-to-downstream energy shifts and wave propagation modulate downstream drought–flood transitions require comprehensive clarification.

To fill this knowledge gap, the present work systematically investigates the early-summer TP QBWOI and its dynamic coupling with South China rainfall using long-term observational and reanalysis datasets. We elucidate how upstream low-frequency background states coordinate to shape downstream extreme precipitation. Ultimately, this work aims to establish a refined conceptual framework for TP-downstream multi-scale interactions, offering fresh physical insights to extend the S2S forecasting window.

## 2. Data and methods

### 2.1. Datasets

The primary atmospheric fields analyzed in this study are derived from the Japanese 55-year Reanalysis (JRA-55) product developed by the Japan Meteorological Agency (Kobayashi et al., 2015). We utilize daily-mean atmospheric variables covering the 42-year period from1979 to 2020, extracted across multiple standard vertical pressure levels on a uniform 1.25° × 1.25° horizontal grid. The primary diagnostic parameters include three-dimensional wind vectors ($u$, $v$, $\omega$), air temperature ($T$), specific humidity ($q$), and geopotential height ($H$).

To characterize the downstream hydrological response, high-resolution daily precipitation records are obtained from the CN05.1 gridded observation dataset (0.25° × 0.25° resolution), which was constructed via spatial interpolation of 2416 surface meteorological stations across China (Wu and Gao, 2013). Additionally, grid-based population density data are acquired from the Global Human Settlement Population (GHS-POP R2023A) provided by the Copernicus Human Settlement platform. To align with our study period, population fields are sampled at five-year intervals from 1975 to 2020 at their native spatial resolution of 30 arc-seconds (~1 km).

### 2.2. Methods

To quantify the subseasonal thermal forcing over the TP, the vertically integrated apparent heat source ($<Q_1>$) from the surface to the 100 hPa level is calculated using the thermodynamic residual budget approach(Yanai, 1961) based on the JRA-55 atmospheric fields. To isolate the subseasonal signals from the daily JRA-55 variables, the climatological annual cycle is first subtracted from the raw records to derive daily anomalies. A 5-day running mean filter is subsequently applied to these daily anomalies to effectively suppress high-frequency weather noise (Yang et al., 2010). Then a Lanczos band-pass filter (Duchon, 1979) is implemented to extract the 10–20-day fluctuations.

Following the approach outlined by Teng and Wang (2003) and Zhu et al. (2025), the variance of the first principal component (PC1) of June 10–20-day filtered $<Q_1>$ is calculated to define the yearly TP QBWOI index, indicating the intensity of QBWO activity over the TP. The interannual component of this intensity metric is subsequently isolated via a 2–7-year band-pass filter, where years exceeding (falling below) ±1.0 standard deviation are classified as typical strong (weak) TP QBWOI regimes. Further, within these designated regimes, active subseasonal events are systematically screened based on the criteria that both the peak and trough amplitudes within a single full cycle must exceed a threshold of ±0.75 standard deviation, yielding a total of 7 robust events in strong years and 6 in weak years. Finally, a complete life cycle of each selected active event is partitioned into eight distinct phases: Phases 1 and 5 correspond precisely to the wave trough and peak of the QBWO cycle, respectively, while Phases 3 and 7 serve as the transitional nodes.

A localized wave energetics framework is utilized to examine the maintenance process of the QBWO signals under different intensity regimes. By diagnosing the interactions between the background climatological flow and the subseasonal eddies, the column-integrated barotropic kinetic energy conversion ($CK$) and baroclinic available potential energy conversion ($CP$) are quantified (Kosaka et al., 2009; Kosaka and Nakamura, 2006):

$$CK = \frac{v''^2 - u''^2}{2}\left(\frac{\partial \overline{u}}{\partial x} - \frac{\partial \overline{v}}{\partial y}\right) - u''v''\left(\frac{\partial \overline{u}}{\partial y} + \frac{\partial \overline{v}}{\partial x}\right) \quad (1)$$

$$CP = -\frac{f}{S}\left(v''T''\frac{\partial \overline{u}}{\partial p} - u''T''\frac{\partial \overline{v}}{\partial p}\right) \quad (2)$$

where the static stability parameter S is defined as:

$$S = \frac{R\overline{T}}{C_p P} - \frac{\partial \overline{T}}{\partial p} \quad (3)$$

The double primes ($''$) exclusively isolate the 10–20-day band-pass filtered subseasonal perturbations. The physical constants denote the Coriolis parameter ($f$), the specific heat at constant pressure ($c_p$), and the gas constant for dry air ($R$). Mechanistically, positive values of $CK$ ($CP$) identify a dynamic upscale energy transfer, wherein the QBWO perturbations extract kinetic (available potential) energy from the background mean flow. Conversely, negative values represent a downscale

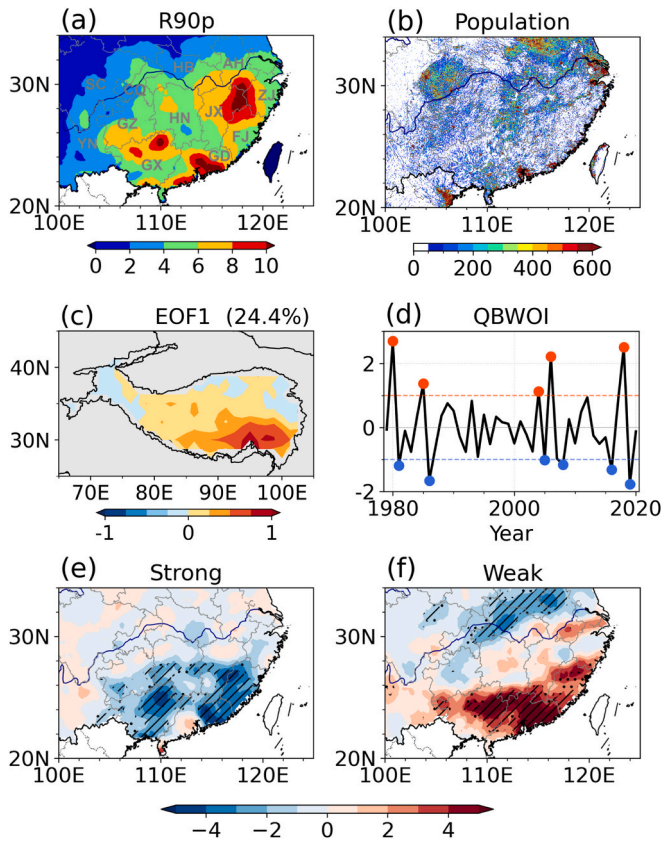



**Fig. 1.** Interannual relationship between TP QBWOI and June extreme precipitation over South China (1979–2020). (a) Climatological June extreme precipitation (*R90p*, mm day$^{-1}$) over South China. (b) Population density (persons·grid$^{-1}$) in South China. (c) First EOF mode (EOF1) of 10–20-day filtered $<Q_1>$ over the TP, with explained variance in parentheses. (d) Normalized 2–7-year bandpass-filtered June TP QBWOI index (black line). Dashed lines indicate ±1.0 standard deviation thresholds separating strong (orange dots) and weak (blue dots) years, respectively. (e, f) Composite June extreme precipitation (mm day$^{-1}$) during (e) strong and (f) weak TP QBWOI years. Slanted hatching and stippling indicate regions exceeding the 95% and 90% statistical significance levels, respectively. (For interpretation of the references to colour in this figure legend, the reader is referred to the web version of this article.)

dissipation of eddy energy back into the climatological mean flow.

To quantitatively elucidate the hydrological sources and physical mechanisms governing the South China extreme precipitation anomalies, a vertically integrated moisture budget framework is applied from the surface up to the 100 hPa level. The generalized anomalous moisture conservation equation is formulated as follows:

$$P' - E' = -\langle \overline{\omega}\partial_p q' \rangle - \langle \omega' \partial_p \overline{q} \rangle - \langle \overline{\vec{V}} \cdot \nabla_h q' \rangle - \langle \vec{V}' \cdot \nabla_h \overline{q} \rangle + Res \quad (4)$$

where $P$ and $E$ represent precipitation and evaporation anomalies, respectively; $q$ is specific humidity, $V$ denotes the horizontal wind vector, and *Res* encompasses the non-linear residual terms. The angle brackets $<\cdot>$ signify the mass-weighted vertical integration from surface to 100 hPa. The overbars designate the climatological mean state averaged over the 1979–2020 period, while the primes indicate the isolated 2–7-year interannual anomalies. To separate circulation-driven features from moisture-driven variations, the anomalous moisture advection terms are further decomposed into thermodynamic and dynamic components. The components primarily dependent on atmospheric thermal states ($-\langle \overline{\omega}\partial_p q' \rangle$ and $-\langle \overline{\overline{\vec{V}}} \cdot \nabla_h q' \rangle$) represent the thermodynamic contributions to regional rainfall fluctuations. Conversely, the components governed by changes in atmospheric circulation ($-\langle \omega' \partial_p \overline{q} \rangle$ and $-\langle \overline{\vec{V}}' \cdot \nabla_h \overline{q} \rangle$, referred to as dynamic elements) dictate the dynamic contributions altering downstream extreme precipitation outcomes (Sheng et al., 2023).

To ensure statistical rigor, all statistical significance levels are evaluated by explicitly adjusting for the effective degrees of freedom (Bretherton et al., 1999).

## 3. Linkage between June South China extreme rainfall and TP QBWOI

To intuitively illustrate the socioeconomic stakes of regional climate anomalies and establish the exposure of human systems, the climatological background of June extreme precipitation (R90p) over South China is first examined alongside local population density (Figs. 1a, b). As shown in Fig. 1a, South China as a whole is characterized by copious rainfall during June. Superimposed on this broad rainy background, three exceptionally prominent extreme precipitation centers are identified, distributed over northern Guangxi, central-coastal Guangdong, and Jiangxi. Crucially, these climatological high-risk precipitation centers overlap directly with, or sit adjacent to, some of the most densely populated and economically developed clusters in China (Fig. 1b), particularly in Guangdong where the local population density exceeds 600 persons·grid$^{-1}$. This spatial coincidence of high hazard risk and dense population exposure implies that subseasonal low-frequency variability can substantially amplify socioeconomic vulnerability, potentially escalating localized heavy rainfall into severe disasters.

To identify upstream subseasonal thermal forcing pathways, an Empirical Orthogonal Function (EOF) analysis was performed on the continuous 10–20-day bandpass-filtered daily vertically integrated atmospheric apparent heat source ($<Q_1>$) over the TP using June daily samples (1979–2020). The leading mode (EOF1), explaining 24.4% of the total variance, exhibits a spatially coherent monopolar structure across the TP, with its primary center situated over the southeastern flank of the TP (Fig. 1c). EOF2 explains 17.4% of the total variance, and the two modes are statistically separable according to the North et al. (1982) criterion. To quantify the interannual intensity variations of QBWO signals, a June TP QBWOI index was constructed by calculating the yearly temporal variance of the June PC1 time series and applying a 2–7-year bandpass filter, thereby isolating its pure interannual recurrent signals (Fig. 1d). Utilizing a threshold of ±1.0 standard deviations ($\pm 1.0\sigma$), five typical strong QBWOI years (1980, 1985, 2004, 2006, and 2018) and six weak years (1981, 1986, 2005, 2008, 2016, and 2019) are isolated as contrasting background climate regimes. Within these strong and weak background years, individual active 10–20-day QBWO cycles are further identified when their wave amplitudes exceed $\pm 0.75\sigma$, yielding 7 and 6 robust subseasonal events, respectively (see details in Section 2.2). Sensitivity tests using alternative thresholds ($\pm 0.5\sigma$ and $\pm 1.5\sigma$) confirm that the composite extreme precipitation anomalies over South China are highly robust against regime-classification criteria (Fig. S1). For simplicity, the subsequent event-based composite analyses hereafter are referred to by their corresponding background regimes (i.e., strong vs. weak QBWOI years), providing a solid statistical baseline for diagnosing downstream anomalies and tracking their divergent subseasonal propagation tracks.

The downstream climatic variations concurrent with the TP thermal anomalies are further elucidated through composite extreme precipitation anomalies during contrasting QBWOI years (Figs. 1e, f). South China's extreme precipitation displays a distinct out-of-phase relationship with the upstream TP QBWOI. During strong QBWOI years (Fig. 1e), a prominent negative precipitation anomaly belt spans across South China, with the maximum deficit exceeding −4 mm day$^{-1}$ over Guangdong and Guangxi, passing the 95% significance level. Conversely, during weak years (Fig. 1f), South China is dominated by significant, widespread positive precipitation anomalies, with wet

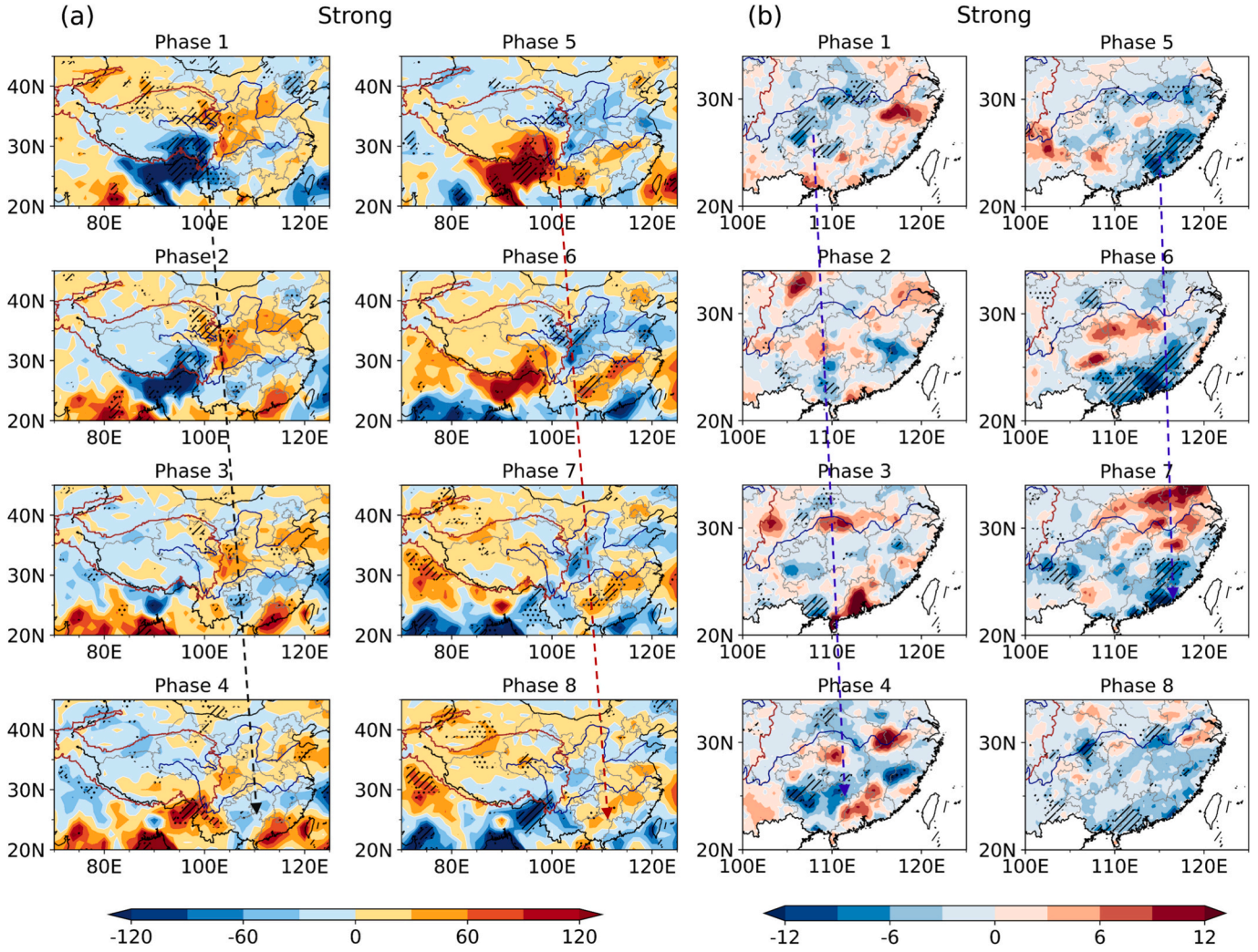



**Fig. 2.** Phase-by-phase evolution of the TP QBWO signals and South China extreme precipitation anomalies (Phases 1–8) during strong TP QBWOI years. (a) Composite 10–20-day filtered $<Q_1>$ anomalies (W $m^{-2}$) over the TP and adjacent regions. (b) Corresponding composite June extreme precipitation anomalies (mm $day^{-1}$) over South China. Slanted hatching and stippling mark significance at the 95% and 90% confidence levels, respectively. Dashed arrows track the propagation of negative (black) and positive (red) QBWO anomalies, as well as the shift in extreme precipitation anomalies (blue). (For interpretation of the references to colour in this figure legend, the reader is referred to the web version of this article.)

anomalies surpassing 4 mm $day^{-1}$ along the southeastern coast. Remarkably, the spatial configurations of these positive and negative anomalies exhibit an exact geographical alignment with the climatological rainfall centers shown in Fig. 1a. This striking contrast implies a close statistical co-variability, wherein a strong TP thermal oscillation corresponds to a suppressed pre-flood extreme rainfall state in South China, whereas a weakened TP QBWO state aligns with an amplified rainfall regime. This clear phase-locking and significant co-fluctuation from the upstream TP to downstream economic centers reinforce the robust teleconnection between interannual variations of intrinsic TP QBWO activity and regional regime shifts between drought and flood conditions over South China.

## 4. Phase evolution of TP QBWO and associated South China extreme rainfall

To examine the dynamic propagation and downstream signal transmission, the continuous phase-by-phase progression of both the upstream TP thermal perturbations (Figs. 2a and 4a) and the corresponding South China extreme precipitation anomalies (Figs. 2b and 4b) are tracked. A complete cycle of the QBWO events is systematically divided into eight phases, with its minimum in Phase 1 and peaks in Phase 5. The contrasting evolutionary tracks during typical strong (Fig. 2) and weak (Fig. 4) TP QBWOI years are scrutinized to examine how the shifting spatial manifestations of the TP QBWO align with the downstream steering and the sequential variations in rainfall anomalies.

During typical strong QBWOI years (Fig. 2), subseasonal signaling exhibits a highly structured, southeastward-directed propagation corridor. As shown in Fig. 1c, the primary center of the QBWO is firmly anchored along the southeastern flank of the TP. Correspondingly, during Phase 1, prominent negative QBWO anomalies dominate this southeastern slope (Fig. 2a). From Phase 2 onward, this anomalous center exhibits a clear eastward and southeastward migration out of the TP margin, encroaching upon the adjacent Southwest China. Despite temporary structural realignments, the structurally coherent low-frequency wavefront successfully propagates northeastward into the region south of the Yangtze River Basin by Phase 3 (Fig. S2). Intriguingly, this northeastward propagation component becomes exceptionally conspicuous during the second half of the evolutionary lifecycle (Phases 5–7). Upon migrating out of the TP during Phase 5, the upstream positive perturbation rapidly coalesces with the existing anomalies over the Yangtze River Valley, establishing a distinctive southwest-to-northeast slanted band, along which low-frequency wave energy exhibits a clear northeastward progression and intensification. Thereafter,

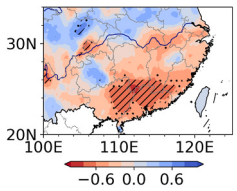



**Fig. 3.** Lead-lag correlation coefficients between the TP QBWOI and June extreme precipitation over South China, with the QBWOI leading precipitation by 8 days. The hatched and dotted shadings denote the regions exceeding the 95% and 90% confidence levels, respectively.

the wave signal steers southward, systematically advancing toward the South China coast during Phases 2–3 (and symmetrically for the opposite phase during Phases 6–7) before undergoing in situ dissipation. This spatial coherence demonstrates that despite localized structural adjustments, positive and negative QBWO phases share a fundamentally consistent downstream propagation pathway throughout their lifecycles.

Concurrent with this upstream QBWO evolution, June extreme precipitation anomalies over South China exhibit a striking, continuous cyclic transition (Fig. 2b), demonstrating a high spatiotemporal coherence with the propagating wave signals. During Phase 1, a statistically significant negative precipitation anomaly is centered south of the Yangtze River Basin. Subsequently, complying with the dynamic steering of the propagating TP QBWO signal, this suppressed precipitation belt systematically migrates southward (guided by the blue dashed line). This continuous downstream propagation culminates in a widespread, statistically significant rainfall deficit over the South China coastal economic hub (20°N − 25°N) during Phase 6, representing the peak suppressed phase of the precipitation lifecycle.

This precise phase alignment suggests a highly regular downstream transmission, requiring approximately four phases (~8 days) for the subseasonal signal to advance from the eastern edge of the TP (Phase 2) to the downstream South China coast (Phase 6). This timescale is robustly corroborated by the lead-lag correlation analysis, which identifies a peak statistically significant negative correlation ($r < -0.6$, passing the 95% confidence level) when the TP QBWOI leads South China extreme precipitation by 8 days (Fig. 3). Spatially, this maximum correlation band is firmly anchored over the coastal region of South China, aligning seamlessly with both the climatological rainfall centers (Fig. 1a) and the composite deficit during Phase 6 (Fig. 2b). This significant lead-lag relationship establishes a highly predictable subseasonal teleconnection between TP low-frequency thermal states and South China rainfall anomalies, reinforcing the composite regime shifts documented in Figs. 1e, f.

Intriguingly, during typical weak years (Fig. 4), the conventional southern-flank signaling becomes strikingly disrupted, which fundamentally explains the weakened overall QBWOI index. Instead of being centered over the southeastern slopes, the subseasonal perturbations

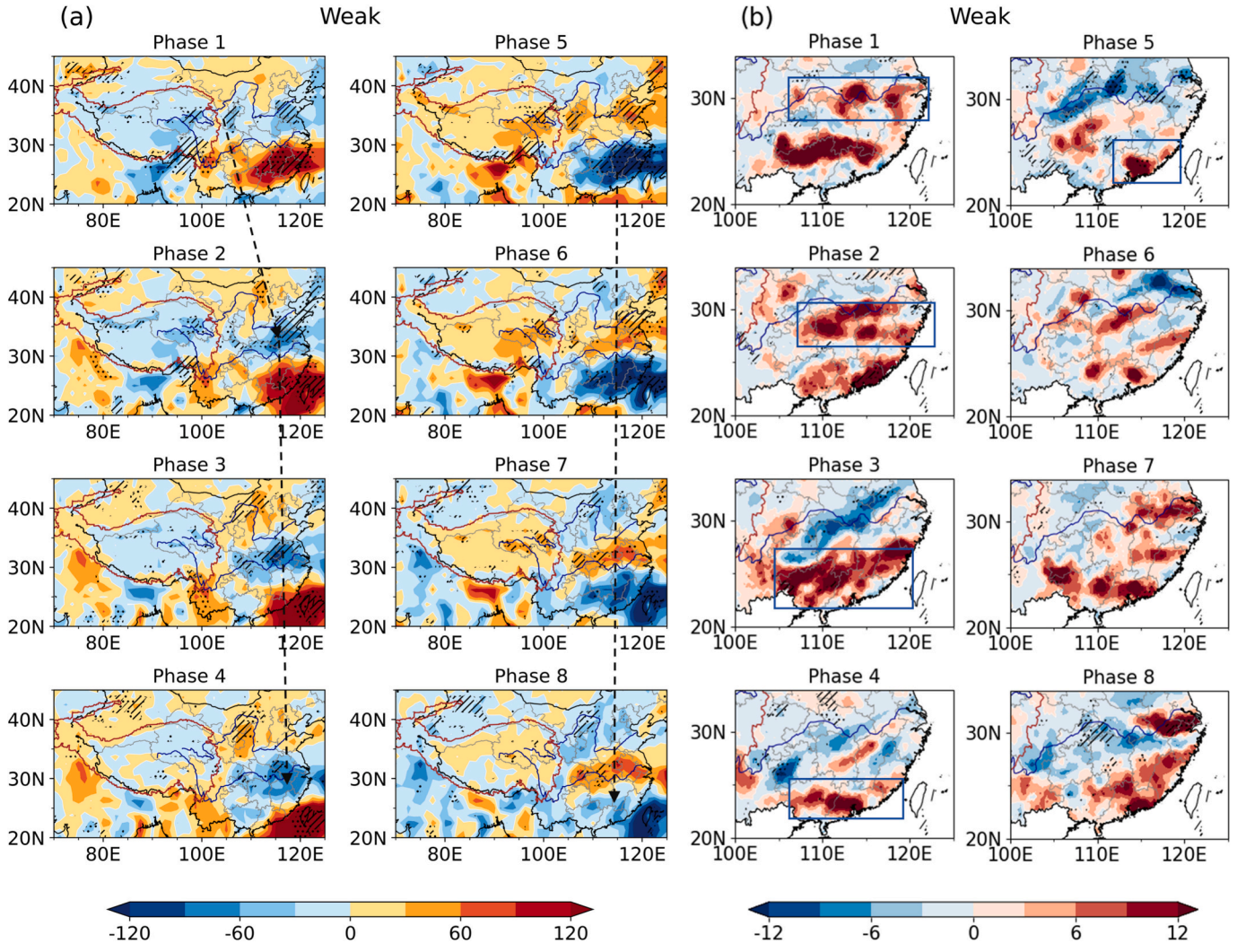



**Fig. 4.** As in Fig. 2, but for typical weak TP QBWOI years.

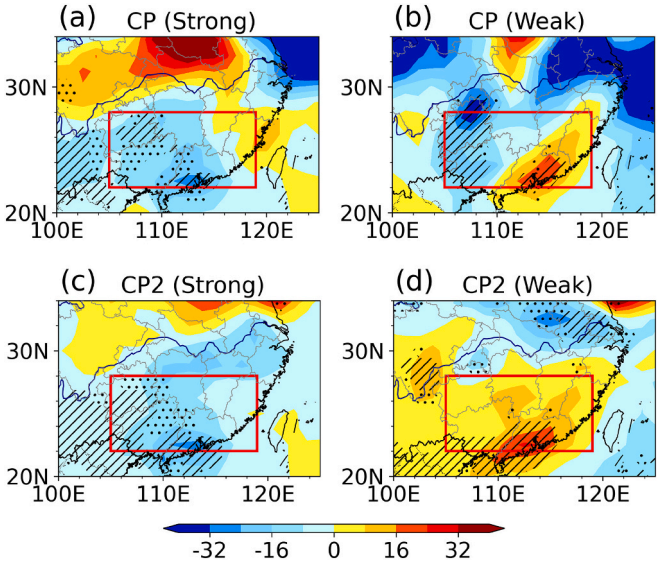



**Fig. 5.** Cross-scale energy conversions over South China during strong and weak TP QBWOI years. (a, b) Vertically integrated baroclinic energy conversion (*CP*) and (c, d) its second component *CP2* ($10^{-4}$ $m^2s^{-3}$ $hPa^{-1}$). Red boxes denote the key region (22°-28°N, 105°-119°E). Slanted hatching and stippling mark significance at the 95% and 90% confidence levels, respectively. (For interpretation of the references to colour in this figure legend, the reader is referred to the web version of this article.)

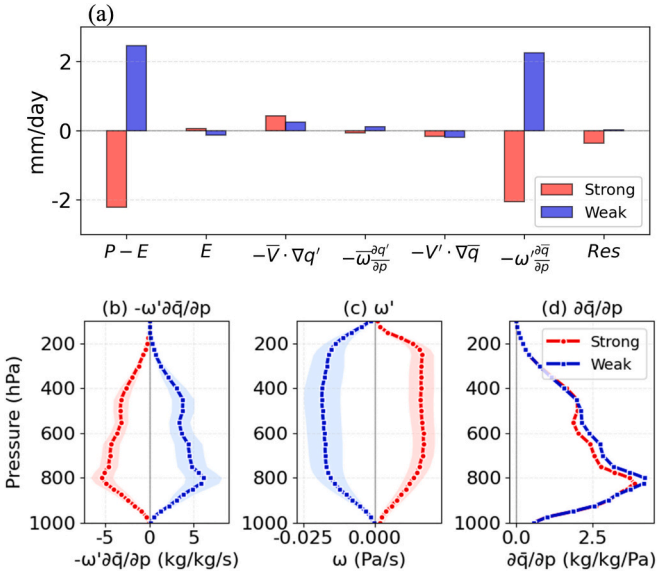



**Fig. 6.** Moisture budget diagnostics over South China during strong and weak TP QBWOI years. (a) Domain-averaged column-integrated moisture budget terms (mm $day^{-1}$). (b-d) Vertical profiles over the key region for (b) vertical dynamic advection $-\omega'\frac{\partial\overline{q}}{\partial p}$ (kg $kg^{-1}$ $s^{-1}$), (c) anomalous vertical velocity $\omega'$ (Pa $s^{-1}$), and (d) background vertical moisture gradient $\frac{\partial\overline{q}}{\partial p}$ (kg $kg^{-1}$ $Pa^{-1}$). Shading in (b, c) represents spatial standard deviation across the key region.

during Phase 1 primarily manifest over the TP interior. From Phase 2 to Phase 3, governed by the northern circumglobal waveguide, these inland perturbations propagate dynamically via a distinct zonal eastward pathway along the mid-latitudes, quickly advancing toward the Yangtze–Huaihe River Basin. Subsequently, from Phase 4 through Phase 6, these QBWO signals shift southward, executing a clear downstream penetration into South China.

Concurrent with this altered upstream evolution, June extreme precipitation anomalies over South China during weak years (Fig. 4b) exhibit a distinct, regime-dependent spatiotemporal manifestation that noticeably differs from the gradual, single-band southward migration observed in strong years. During Phases 1–2, instead of being confined to a localized region, the positive extreme precipitation anomalies present a prominent broad-band distribution firmly established over the Yangtze River Basin. Subsequently, during Phase 3, a substantial spatial reorganization takes place, with an intensified positive precipitation anomaly extending across the South China coast (20°N–25°N). By Phases 4–5, this enhanced convective band systematically migrates further southward and begins to clear the continental coastline, allowing the regional anomalies to weaken or decay in situ during the final phases of the lifecycle.

## 5. The regime-dependent energetic and dynamic mechanisms

To understand physical mechanisms underlying the cross-scale linkages between the TP QBWO and South China extreme precipitation, a rigorous atmospheric energetic diagnosis is applied to the regional energy conversion processes over South China during both typical strong and weak TP QBWOI years (Fig. 5). Our diagnostic results reveal that the subseasonal wave energetics along the pathway are overwhelmingly dominated by baroclinic processes (*CP*), whereas the barotropic energy conversion (*CK*) is more than one order of magnitude smaller than the *CP* and thus plays a secondary role (Fig. S3). Fundamentally, *CP* emerges as the leading contributor, with its second component, *CP2*, emerging as the leading contributor (Fig. 5 and Fig. S3). Dynamically, these two terms quantify the baroclinic conversion efficiency between the background mean available potential energy and low-frequency eddy perturbations. Mechanistically, a positive *CP* sign characterizes a dynamic extraction of available potential energy from the monsoonal background to fuel local perturbations, whereas a negative sign implies a thermodynamic dampening on the subseasonal waves.

Specifically, during strong TP QBWOI years, the key domain over South China exhibits prominent and statistically significant negative values for both *CP* and *CP2* (Figs. 5a, c). This widespread energetic deficit indicates that as TP QBWO signals propagate downstream toward South China, regional energy allocation aligns with a significant attenuation of eddy potential energy, restricting the maintenance of their low-frequency dynamic columns. Concurrent with this energetic deficit, localized convective disturbances are heavily suppressed, which is highly consistent with the pronounced negative anomalies of extreme precipitation observed over South China during these strong years.

In contrast, during weak TP QBWOI years, the downstream energetic regime over South China undergoes a profound thermodynamic realignment, exhibiting a distinctive spatial inhomogeneity (Figs. 5b, d). Instead of a uniform enhancement, a striking contrast is established within the target domain: a localized negative conversion center occupies the northwestern flank, whereas extensive and statistically significant positive values of both *CP* and *CP2* firmly anchor over the southeastern coastal ribbon and adjacent maritime gateways. Importantly, for CP2 (Fig. 5d), positive energy conversion values dominate across nearly the entire key domain, with the maximum significant center aligned along the southern coast. This systematic shift in the coastal region demonstrates that during a weakened upstream forcing state from the TP, the East Asian monsoonal background flow aligns with an active release of available potential energy, encouraging localized subseasonal disturbances via classical baroclinic instability. Under this background regime, subseasonal convective perturbations and regional thermal instabilities are co-amplified. Because the atmospheric column is systematically destabilized by this positive baroclinic feedback, the regional convective environment becomes more variable, consistent with the prominent positive anomalies of localized extreme precipitation across South China.

The regional energy diagnostics (Figs. 5a–d) elucidate how cross-

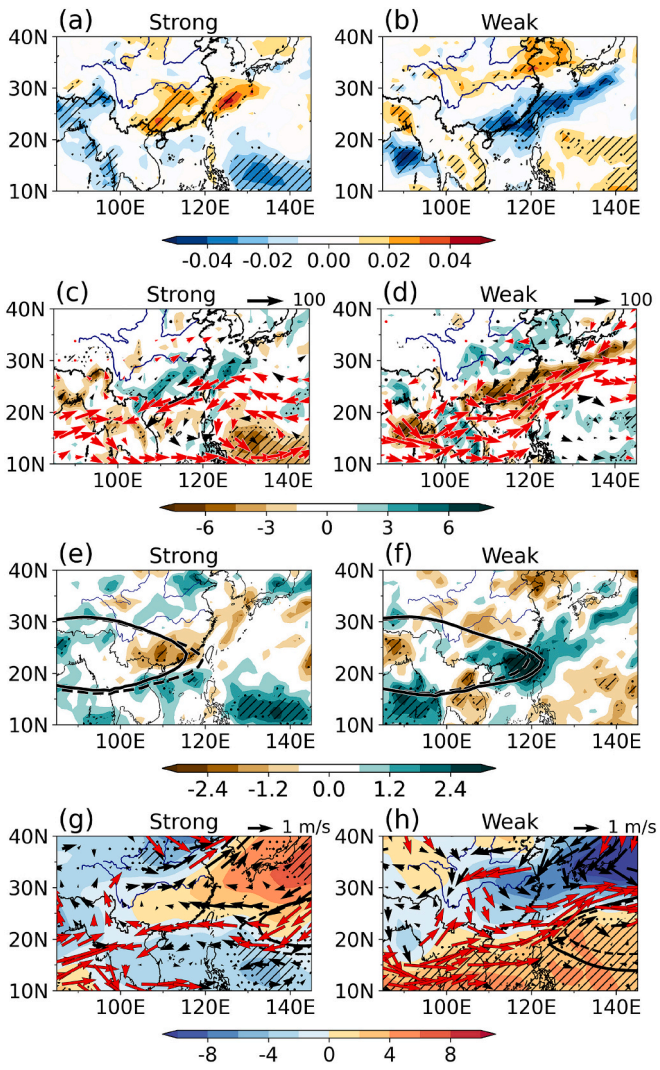



**Fig. 7.** Large-scale atmospheric circulation composites over East Asia and conceptual mechanisms for June South China extreme precipitation during strong (left) and weak (right) TP QBWOI years. (a, b) 500-hPa vertical velocity (Pa $s^{-1}$). (c, d) Vertically integrated moisture flux (vectors; kg $m^{-1}$ $s^{-1}$) and its divergence (shading; $10^{-5}$ kg $m^{-2}$ $s^{-1}$). (e, f) 200-hPa divergence (shading; $10^{-6}$ $s^{-1}$) and South Asia High (SAH; 12,500-gpm contours). (g, h) 500-hPa geopotential height anomalies (shading; gpm) and Western Pacific Subtropical High (WPSH; 5880-gpm contours). Solid (dashed) contours in (e–h) denote composite (climatological) boundaries. Red vectors, slanted hatching, and stippling mark 95% significance for vectors, shading (95%) and shading (90%), respectively. (For interpretation of the references to colour in this figure legend, the reader is referred to the web version of this article.)

scale conversions align with subseasonal wave intensity, while the moisture-budget analysis examines the interannual rainfall environment associated with the same regime classification and event sampling. Since the ultimate realization of extreme precipitation anomalies is closely linked to vertical motion and moisture transport, a column-integrated moisture budget analysis was conducted over South China (Fig. 6a). Following Teng and Wang (2003) and Sheng et al. (2023), anomalous moisture processes are decomposed into a circulation-driven dynamical component and a moisture-driven thermodynamic component. The column-integrated net anomalous ($P - E$) exhibits a profound interannual reversal, with a massive suppression ($-2.2$ mm $day^{-1}$) during strong years and a sharp enhancement (2.4 mm $day^{-1}$) during weak years. Notably, the evaporation ($E$) and residual terms ($Res$) remain negligible across both regimes, confirming a highly closed hydrological balance.

Among all budgetary terms, the vertical dynamic advection term ($-\omega'\frac{\partial\overline{q}}{\partial p}$) emerges as the dominant component, tracking the total $P - E$ signal with striking fidelity. While horizontal moisture advection ($-\vec{V}\bullet\nabla q'$) yields a minor positive contribution during strong years, it is overwhelmingly exceeded by the vertical dynamical term. This indicates that South China extreme precipitation anomalies are strictly coupled with circulation-driven vertical dynamics rather than changes in mean moisture availability or surface evaporation. It should be noted, however, that because vertical motion and deep convection are inherently tied through latent heat release and diabatic feedbacks, this moisture diagnostic highlights a strong dynamical co-variability and tight thermodynamic-dynamic coupling, rather than a strictly linear cause-and-effect relationship.

Vertical profiles further isolate the fine structures of this key dynamic component (Figs. 6b–d). Crucially, the background vertical moisture profile ($\frac{\partial\overline{q}}{\partial p}$) is virtually identical between the strong and weak configurations (Fig. 6d), with both peaking near 800 hPa ($\sim$4 kg $kg^{-1}$ $Pa^{-1}$). This thermodynamic homogeneity demonstrates that local water vapor capacity is abundantly available and not a limiting factor for regional extremes. Consequently, the interannual precipitation reversal is tightly gated by anomalous vertical velocity anomalies (ω'): prominent anomalous descending motions ($\omega' > 0$) during strong years systematically suppress moisture convergence, whereas vigorous ascending motions ($\omega' < 0$) during weak years are most pronounced in the lower-to-mid troposphere (800–600 hPa, Figs. 6b and c). The robust separation between the confidence intervals (shaded envelopes) of strong and weak regimes further underlines the statistical stability of this vertical motion pump. This dominant role of the dynamical vertical motion pump aligns seamlessly with recent extreme rainfall studies over South China (Sheng et al., 2023).

To contextualize the anomalous dynamic pump (ω') over South China, the composite large-scale atmospheric configurations during typical strong and weak years are examined (Fig. 7). In the upper troposphere, a highly synchronized dynamic coupling operates between 200-hPa divergence anomalies and the South Asia High (SAH) configuration. During strong TP QBWOI years, South China aligns with anomalous 500-hPa descending motions (exceeding 0.02 Pa $s^{-1}$; Fig. 7a). This vertical suppression concurs with a prominent northwestward shift and retreat of the SAH core relative to its climatological position over the East Asian margins (Fig. 7e), which places South China under the unfavorable downstream convergent periphery of the upper-level anticyclone. This upper-level displacement induces a widespread anomalous 200-hPa convergence zone (shading in Fig. 7e) and weakens the local dynamic suction, collectively suppressing convective amplification via deep subsidence.

Conversely, during weak years, a robust 500-hPa ascending anomaly is established over South China (Fig. 7b), closely coupled with a substantial enhancement of 200-hPa divergence (shading in Fig. 7f). Here, the SAH exhibits an eastward shift and southward extension, with its composite eastern ridge overriding the 120°E meridian and directly overlying South China (Fig. 7f). This configuration forms a favorable upper-level divergent environment that acts as an effective dynamic suction pump, providing the prerequisite upper-level pulling force to accommodate the deep upward-pumping dynamic column.

This upper-level environment is highly coordinated with the low-to-mid-tropospheric circulation and moisture conveyor belts (Figs. 7c, d, g, h). During strong years, the low-to-mid-tropospheric environment is characterized by a distinct eastward and northward retreat of the WPSH, with its composite 5880-gpm line withdrawing notably toward the maritime basin (Fig. 7g). Consequently, South China is positioned on the southwestern flank of an anomalous anticyclonic circulation, dominated by low-level easterly anomalies and widespread moisture divergence (Figs. 7c and S4a). This circulation setup effectively blocks the penetration of warm, moist tropical air masses into the subtropical regions,

depriving South China of the moisture supply necessary for sustained heavy rainfall.

In sharp contrast, during weak years, the background circulation undergoes a profound realignment. The WPSH shifts significantly westward and southward, while a prominent anomalous cyclonic pump is established at 500-hPa over the middle-to-lower reaches of the Yangtze River (Fig. 7h). Embedded in this cyclonic anomaly and flanking the shifted WPSH, South China is governed by a robust channel of anomalous southwesterly winds that continuously transport moisture from the Bay of Bengal and the South China Sea, creating a statistically significant moisture convergence regime (Figs. 7d and S4b). The intersection between these intensified monsoonal inflows and the southern periphery of the 500-hPa cyclonic anomaly provides both sustained moisture supplies and strong dynamic lifting, directly promoting a positive *CP* conversion and thereby explaining the extensive spatiotemporal organization of the downstream extreme precipitation anomalies.

## 6. Discussions

To substantiate the robust existence of these regime-dependent pathways, the conceptual framework is projected onto two highly representative cases: June 1980 (a typical strong TP QBWOI event) and June 1986 (a typical weak TP QBWOI event) (Figs. S5 and S6). The spatiotemporal evolutions of observed TP QBWO anomalies and extreme precipitation patterns closely mirror the corresponding composites. In June 1980 (Fig. S5a), the subseasonal thermal signal propagates along the southern flank of the TP, driving severe precipitation deficiencies along the South China coast during Phases 5–6 (Fig. S6a). In contrast, June 1986 (Fig. S5b) exemplifies the inland eastward pathway. An isolated subseasonal thermal cluster emerges within the interior TP core, propagates due east, and facilitates rapid zonal landfall over the Yangtze–Huaihe Basin by Phase 3, followed by a spatial consolidation over South China during Phases 3–4 (Fig. S6b). Crucially, energetic diagnostics demonstrate that the spatial distributions of local baroclinic energy conversions show striking agreement with our composite regimes (Fig. S7), confirming that this upstream regulation represents a structurally stable, dynamically recurring mode within the Asian summer monsoon system.

A fundamental question arises as to what physically dictates these contrasting wave propagation pathways between strong and weak regimes. Our steering flow analysis suggests that this divergence is primarily driven by the latitudinal displacement of the initial TP QBWO thermal source (30°N vs. 35°N) interacting with the quasi-stationary background flow (Fig. S8). As shown by the background wind vectors, a robust, straight westerly flow dominates the mid-latitude zone (35°N–40°N). During weak years, because the QBWO active center originates over the TP interior (~35°N), it is directly embedded within this straight zonal flow, driving the subseasonal wave energy due east along a parallel trajectory. In sharp contrast, during strong years, the QBWO active center is anchored along the southern flank of the TP (~30°N). This latitudinal zone coincides precisely with the northeastern periphery of the SAH (Fig. 7e and f), where the upper-level flow exhibits a distinct equatorward/southeastward dip over the eastern flank of the TP (100°E–120°E; Fig. S8a). Governed by this anticyclonic steering component at 30°N, the subseasonal perturbations are guided southeastward toward lower latitudes. Thus, the regime-dependent propagation pathways are essentially governed by whether the initial upstream perturbation is triggered within the straight mid-latitude zonal flow (35°N) or within the equatorward-curving steering flow along the SAH's northeastern flank (30°N).

The present results are partly consistent with previous findings by Zhu et al. (2025, 2026), who reported interannual co-variability between TP QBWOI and local/downstream summer precipitation over China. This study extends that understanding by demonstrating that two distinct propagation regimes exist under strong versus weak QBWOI background states, highlighting the energetic-dynamic gating effect that was not emphasized in earlier work. Although many prior studies (e.g., Wang et al., 2019) provided a generalized climatological eastward propagation of TP subseasonal signals, the present analysis indicates that the actual propagation pathways differ significantly depending on background intensity: the classic southeastward propagation occurs preferentially in strong QBWOI years, whereas weak-year signals route zonal-eastward. This shift from climatological mean features to interannual intensity variability resolves the discrepancies with earlier literature.

To further verify the structural robustness of these findings, sensitivity tests by iteratively omitting one- or two-year combinations confirm that the composite patterns remain qualitatively invariant, ensuring that the identified mechanisms are not artifacts of isolated extreme years. These diagnostic outcomes support the stability of the regional-mean sign, while indicating minor sensitivity of the amplitude and spatial structure to some year combinations.

A critical fundamental issue concerns the causal hierarchy between the TP QBWOI, the large-scale atmospheric circulation configurations (Fig. 7), and broader climate drivers. Statistical diagnostics alone cannot completely isolate whether the broad-scale circulation anomalies are generated by the TP ISO or forced simultaneously by broader climate modes (e.g., ENSO, Indian Ocean Dipole) (Yu et al., 2022, 2025). Therefore, rather than asserting a strict causality, these multiscale interactions are more appropriately framed as robust associated changes and co-variations. Within this multi-scale monsoon framework, broader climate drivers and circulations provide the favorable background environment, while the TP QBWO serves as the active subseasonal perturbation and energy carrier. The large-scale circulation patterns and the TP ISO operate jointly modulating the energy conversion and convective regimes over downstream South China. Future studies utilizing dedicated numerical sensitivity experiments will be essential to disentangle the precise feedback loops between subseasonal TP heating and these broader climate modes.

From a multi-scale perspective, this low-frequency background provides a physical bridge to cascade into localized hazards by modulating downstream thermodynamic and kinematic frameworks. The weak-year macro-scale configurations optimize vertical wind shear profiles and enhance local convective available potential energy (CAPE) via sustained moisture convergence, thereby reducing the venting effect on nascent cells and facilitating the upscale growth of embedded disturbances into widespread heavy-rainfall clusters(Chen et al., 2022; Feng et al., 2019). Conversely, the deep subsidence characteristic of strong years systematically erodes local CAPE and disrupts storm longevity.

This structural stability delivers a robust physical baseline and uncovers a critical prognostic indicator for S2S forecasting: the upstream TP thermal precursor leads downstream South China extreme precipitation by approximately 8 days (four phases). This explicit 8-day lead-lag relationship provides a "window of opportunity" for extended-range predictive systems. Rather than treating the TP QBWO as an isolated linear wave, incorporating its slowly varying background intensity into predictive frameworks may enhance forecast skills for downstream climate hazards. Future endeavors utilizing dedicated numerical sensitivity experiments and multi-scale tracking of embedded disturbances (e.g., TP Vortices and mesoscale convective systems) will further quantify these trans-regional cascades and optimize the translation of these upstream precursors into operational subseasonal prediction models.

## 7. Conclusions

This study systematically investigates the non-linear teleconnection between the early-summer TP QBWO and extreme precipitation over South China during 1979–2020. By integrating cross-scale energy diagnostics and column-integrated moisture budgets, we elucidate how

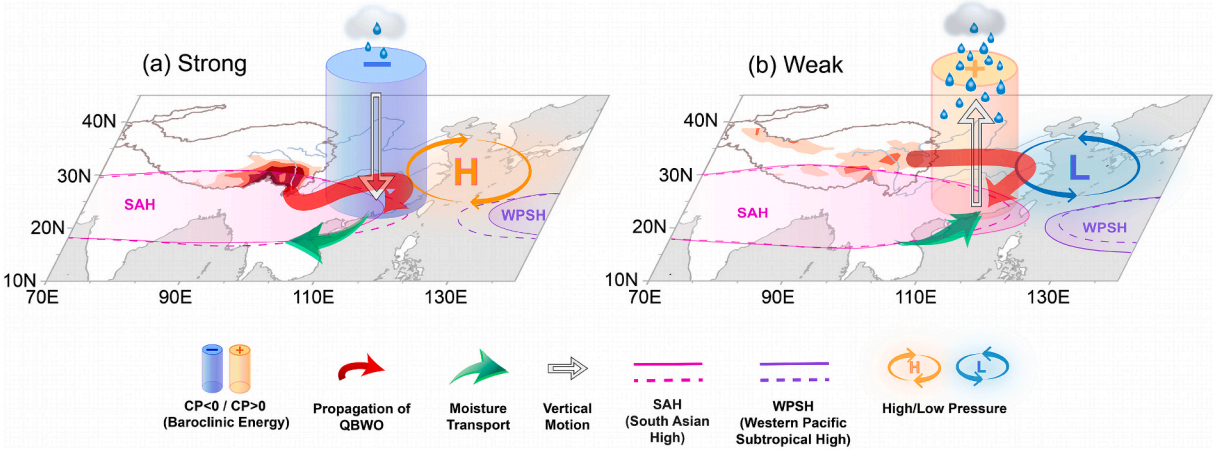



**Fig. 8.** Schematic diagrams illustrating the pathways and large-scale atmospheric configurations associated with June extreme precipitation variations over South China during (a) strong versus (b) weak TP QBWOI years. The blue and yellow cylinders represent the negative and positive baroclinic energy conversion (CP) states, respectively. The red arrows track the downstream propagation pathways of the TP QBWO signals. The green arrows denote the tracks of anomalous moisture transport, while the hollow vertical arrows indicate the anomalous vertical motion (downward versus upward). The dashed and solid pink lines delineate the climatological and the composite boundaries of the South Asian High (SAH, indicated by the 12,500 gpm contour), respectively. Similarly, the dashed and solid purple lines outline the climatological and composite boundaries of the Western Pacific Subtropical High (WPSH, indicated by the 5880 gpm contour). Characters "H" and "L" mark the centers of anomalous high- and low-pressure systems, respectively. (For interpretation of the references to colour in this figure legend, the reader is referred to the web version of this article.)

upstream subseasonal wave signals modulate downstream extreme rainfall, establishing a regime-dependent energetic-dynamic gating framework (Fig. 8). The primary conclusions are summarized as follows:

(1) The interannual modulation of downstream extreme rainfall is fundamentally dictated by the latitudinal position of the upstream TP QBWO thermal precursor (Fig. 8). During strong TP QBWOI years (Fig. 8a), subseasonal perturbations are anchored along the TP's southeastern flank (~30°N), steering southeastward toward South China. Conversely, during weak years (Fig. 8b), the active center shifts to the TP interior (~35°N), initiating a zonal eastward propagation trajectory toward the Yangtze-Huaihe Basin and South China. Crucially, these upstream thermal signals systematically lead downstream South China extreme precipitation anomalies by approximately 8 days (four QBWO phases).
(2) Under strong TP QBWOI years (Fig. 8a), the spatial alignment between the arriving wave path and the background flow yields negative baroclinic energy conversion ($CP < 0$), causing the ISO eddy energy to dissipate back into the climatological mean flow. Structurally, this is orchestrated by an upper-level northwestward withdrawal of the SAH and a low-level eastward retreat of the WPSH, establishing an anomalous high-pressure regime over East Asia that restricts monsoonal moisture transport and suppresses convective growth over South China.
(3) Under weak TP QBWOI years (Fig. 8b), arriving wave perturbations enter a hotbed of positive baroclinic energy conversion ($CP > 0$), where the ISO perturbations dynamically interact with the background flow to extract eddy available potential energy from the mean flow, driving rapid localized eddy amplification. This energetic ignition is seamlessly coupled with an upper-level eastward expansion of the SAH and a low-level westward extension of the WPSH, establishing a low-level cyclonic pump and strong monsoonal moisture conveyor that fuels widespread extreme precipitation over South China.

Together, these findings demonstrate that the downstream impact of the TP QBWO relies crucially on the physical alignment between wave propagation pathways and regional baroclinic regimes. Incorporating these regime-dependent pathways into operational frameworks provides a robust "window of opportunity" for advancing S2S forecasts of climate hazards.

## CRediT authorship contribution statement

**Meirong Wang:** Writing – review & editing, Supervision, Conceptualization, Writing – original draft. **Xuepeng Cui:** Visualization, Methodology, Investigation. **Shunwu Zhou:** Supervision, Writing – review & editing. **Jun Wang:** Writing – review & editing. **Zhu Zhu:** Visualization. **Cong Miao:** Methodology.

## Declaration of competing interest

The authors declare that they have no known competing financial interests or personal relationships that could have appeared to influence the work reported in this paper.

## Acknowledgement

This research has been supported by the National Natural Science Foundation of China (42475129), and Xizang Science and Technology Plan Project (XZ202602YD0006).

## Appendix A. Supplementary data

Supplementary data to this article can be found online at https://doi.org/10.1016/j.atmosres.2026.109439.

## Data availability

The JRA55 reanalysis datasets are freely available through the Japan Meteorological Agency at https://www.data.jma.go.jp/jra/html/JRA-55/index_en.html. The CN05.1 daily observational precipitation dataset can be accessed via the China Meteorological Administration data service platform at https://data.cma.cn/data/cdcindex/cid/f0fb4b55508804ca.html. The Global Human Settlement Population (GHS-POP R2023A) dataset is available from the Copernicus Human Settlement platform at https://human-settlement.emergency.copernicus.eu/.

## References


Bretherton, C.S., Widmann, M., Dymnikov, V.P., Wallace, J.M., Bladé, I., 1999. The effective number of spatial degrees of freedom of a time-varying field. J. Clim. 12, 1990–2009. https://doi.org/10.1175/1520-0442(1999)012%3C1990:TENOSD%3E2.0.CO;2.

Chen, H., Xu, W., Liu, N., Sun, J., Fu, J., 2022. Climatologies of mesoscale convective systems over China observed by spaceborne radars. Mon. Weather Rev. 150, 2697–2717. https://doi.org/10.1175/MWR-D-22-0002.1.

Ding, Q., Wang, B., 2005. Circumglobal teleconnection in the Northern Hemisphere summer. J. Clim. 18, 3483–3505. https://doi.org/10.1175/JCLI3473.1.

Duchon, C.E., 1979. Lanczos filtering in one and two dimensions. J. Appl. Meteorol. Climatol. 18, 1016–1022. https://doi.org/10.1175/1520-0450(1979)018%3C1016:LFIOAT%3E2.0.CO;2.

Fang, H., Qiao, Y., Jian, M., 2023. Dynamic and thermodynamic causes of summer extreme precipitation over South China. Atmos. Res. 293, 106894. https://doi.org/10.1016/j.atmosres.2023.106894.

Feng, T., Wu, H., Lai, S., Huang, B., Hu, Z., Dong, W., Huang, J., 2025. Interdecadal increase of the contribution of extreme precipitation in June in South China. Geophys. Res. Lett. 52, e2025GL117366. https://doi.org/10.1029/2025GL117366.

Feng, Z., Houze, R.A., Leung, L.R., Song, F., Hardin, J.C., Wang, J., Gustafson, W.I., Homeyer, C.R., 2019. Spatiotemporal characteristics and large-scale environments of mesoscale convective systems east of the Rocky Mountains. J. Clim. 32, 7303–7328. https://doi.org/10.1175/JCLI-D-19-0137.1.

Fujinami, H., Yasunari, T., 2009. The effects of midlatitude waves over and around the Tibetan plateau on submonthly variability of the East Asian summer monsoon. Mon. Weather Rev. 137, 2286–2304. https://doi.org/10.1175/2009MWR2826.1.

Gu, W., Wang, L., Hu, Z.-Z., Hu, K., Li, Y., 2018. Interannual variations of the first rainy season precipitation over South China. J. Clim. 31, 623–640. https://doi.org/10.1175/JCLI-D-17-0284.1.

Guo, D., Liu, Y., Wu, G., Mao, J., Jiang, J., Yang, Y., 2024. Generation of the quasi-biweekly oscillation in the surface potential vorticity over the Tibetan Plateau during boreal summer: a case study of 2014. J. Geophys. Res. Atmos. 129, e2024JD041161. https://doi.org/10.1029/2024JD041161.

Guo, D., Sheng, C., Liu, Y., Mao, J., Wu, G., 2025. Interannual variation in quasi-biweekly oscillation intensity of surface potential vorticity over the Tibetan Plateau in summer and its impacts. J. Clim. 38, 5163–5177. https://doi.org/10.1175/JCLI-D-25-0087.1.

Hong, J., Ke, Z., Yuan, Y., Shao, X., 2021. Boreal summer intraseasonal oscillation and its possible impact on precipitation over Southern China in 2019. J. Meteorol. Res. 35, 571–582. https://doi.org/10.1007/s13351-021-0189-9.

Hsu, P.-C., Lee, J.-Y., Ha, K.-J., 2016. Influence of boreal summer intraseasonal oscillation on rainfall extremes in southern China. Int. J. Climatol. 36, 1403–1412. https://doi.org/10.1002/joc.4433.

Hu, W., Duan, A., Wu, G., Mao, J., He, B., 2023. Quasi-biweekly oscillation of surface sensible heating over the Central-Eastern Tibetan plateau and its relationship with spring rainfall in China. J. Clim. 36, 6917–6936. https://doi.org/10.1175/JCLI-D-22-0892.1.

Jin, H., Zhang, K., Liu, M., Yu, X., Yang, X., Chao, L., Zhang, P., Liu, G., 2025. Global Escalation of More Frequent and Intense Compound Heatwave-Extreme Precipitation Events. https://doi.org/10.5194/egusphere-2025-4289.

Khadke, L., Evans, J.P., Kim, Y., Virgilio, G.D., Kala, J., 2026. Observed and projected increases in short-duration extreme precipitation under climate change over Greater Sydney. Environ. Res. Commun. 8, 055013. https://doi.org/10.1088/2515-7620/ae6394.

Kobayashi, S., Ota, Y., Harada, Y., Ebita, A., Moriya, M., Onoda, H., Onogi, K., Kamahori, H., Kobayashi, C., Endo, H., Miyaoka, K., Takahashi, K., 2015. The JRA-55 reanalysis: general specifications and basic characteristics. J. Meteorol. Soc. Jpn. Ser. II 93, 5–48. https://doi.org/10.2151/jmsj.2015-001.

Kong, X., Wang, A., Xue, Y., Wei, N., Zhang, H., Hu, Q., He, J., Bi, X., Chen, Y., 2025. Predicting on the extreme precipitation in east and southeast Asia during summer 2022 from the antecedent soil temperature anomaly over the Tibetan Plateau. J. Clim. 38, 2109–2128. https://doi.org/10.1175/JCLI-D-24-0500.1.

Kosaka, Y., Nakamura, H., 2006. Structure and dynamics of the summertime Pacific–Japan teleconnection pattern. Q. J. R. Meteorol. Soc. 132, 2009–2030. https://doi.org/10.1256/qj.05.204.

Kosaka, Y., Nakamura, H., Watanabe, M., Kimoto, M., 2009. Analysis on the dynamics of a wave-like teleconnection pattern along the summertime Asian jet based on a reanalysis dataset and climate model simulations. J. Meteorol. Soc. Japan. Ser. II 87, 561–580. https://doi.org/10.2151/jmsj.87.561.

Li, J., Mao, J., 2019. Coordinated influences of the tropical and extratropical intraseasonal oscillations on the 10–30-day variability of the summer rainfall over southeastern China. Clim. Dyn. 53, 137–153. https://doi.org/10.1007/s00382-018-4574-8.

Li, Qian, Xue, Y., Kong, X., Lau, W.K.-M., Wang, A., Li, Qiaoping, Cao, Z., Nayak, H., Xu, G., Guo, W., Vasic, R., 2025. Excessive Tibetan Plateau spring warming found to cause catastrophic June 2024 heavy rainfall in China. Sci. Bull. 70, 1596–1600. https://doi.org/10.1016/j.scib.2025.01.011.

Li, X., Wang, D., Zhou, W., 2024. Multiple-time-scale variations of the record-breaking pre-summer rainfall over South China in 2022. J. Clim. 37, 1965–1980. https://doi.org/10.1175/JCLI-D-23-0586.1.

Liu, J., Lu, R., 2022. Different impacts of intraseasonal oscillations on precipitation in southeast China between early and late summers. Adv. Atmos. Sci. 39, 1885–1896. https://doi.org/10.1007/s00376-022-1347-4.

Lu, W., Ha, Y., Zhu, Y., Dai, H., Hu, Y., Yang, X., Liu, Y., Zhong, Z., 2026. Distinct dominant intraseasonal oscillation modes modulate South China's persistent extreme precipitation in rainy season. Geophys. Res. Lett. 53, e2025GL120893. https://doi.org/10.1029/2025GL120893.

Luo, Y., Xia, R., Chan, J.C.L., 2020. Characteristics, physical mechanisms, and prediction of pre-summer rainfall over South China: research progress during 2008–2019. J. Meteorol. Soc. Japan. Ser. II 98, 19–42. https://doi.org/10.2151/jmsj.2020-002.

Miao, R., Wen, M., Zhang, R., Li, L., 2019. The influence of wave trains in mid-high latitudes on persistent heavy rain during the first rainy season over South China. Clim. Dyn. 53, 2949–2968. https://doi.org/10.1007/s00382-019-04670-y.

Myhre, G., Alterskjær, K., Stjern, C.W., Hodnebrog, Ø., Marelle, L., Samset, B.H., Sillmann, J., Schaller, N., Fischer, E., Schulz, M., Stohl, A., 2019. Frequency of extreme precipitation increases extensively with event rareness under global warming. Sci. Rep. 9, 16063. https://doi.org/10.1038/s41598-019-52277-4.

Pan, H., Ren, H.-L., Ma, J., Wang, Y., 2025. Contrasting northward and southward propagations of intraseasonal precipitation under the southern China summer rainfall pattern. Atmos. Res. 314, 107808. https://doi.org/10.1016/j.atmosres.2024.107808.

Qiu, D., Yao, S., Xia, Y., 2022. Pre-summer persistent heavy rain over Southern China and its relationship with intra-seasonal oscillation of tropical atmosphere. J. Trop. Meteorol. 28, 445–456. https://doi.org/10.46267/j.1006-8775.2022.033.

Ren, P., Ren, H.-L., Fu, J.-X., Wu, J., Du, L., 2018. Impact of boreal summer intraseasonal oscillation on rainfall extremes in southeastern China and its predictability in CFSv2. J. Geophys. Res. Atmos. 123, 4423–4442. https://doi.org/10.1029/2017JD028043.

Sheng, B., Wang, H., Li, H., Wu, K., Li, Q., 2023. Thermodynamic and dynamic effects of anomalous dragon boat water over South China in 2022. Weather Clim. Extrem. 40, 100560. https://doi.org/10.1016/j.wace.2023.100560.

Teng, H., Wang, B., 2003. Interannual variations of the boreal summer intraseasonal oscillation in the Asian–Pacific region*. J. Clim. 16, 3572–3584. https://doi.org/10.1175/1520-0442(2003)016%3C3572:IVOTBS%3E2.0.CO;2.

Vitart, F., Robertson, A.W., 2018. The sub-seasonal to seasonal prediction project (S2S) and the prediction of extreme events. Npj Clim. Atmos. Sci. 1, 3. https://doi.org/10.1038/s41612-018-0013-0.

Wang, M., Duan, A., 2015. Quasi-biweekly oscillation over the Tibetan Plateau and its link with the Asian Summer Monsoon*. J. Clim. 28, 4921–4940. https://doi.org/10.1175/JCLI-D-14-00658.1.

Wang, M., Wang, J., Duan, A., Yang, J., Liu, Y., 2019. Quasi-biweekly impact of the atmospheric heat source over the Tibetan Plateau on summer rainfall in Eastern China. Clim. Dyn. 53. https://doi.org/10.1007/s00382-019-04798-x.

Wang, M., Wang, J., Duan, A., Zhou, S., Zhu, Z., Cui, X., Li, J., 2026. Decadal surge in Tibetan Plateau 20–30-day oscillation intensity (1995–2005) linked to summer NAO structure and baroclinic energy conversion. J. Geophys. Res. Atmos. 131, e2026JD047302. https://doi.org/10.1029/2026JD047302.

Xie, J., Hsu, P.-C., Hu, Y., Ye, M., Yu, J., 2023. Skillful extended-range forecast of rainfall and extreme events in east China based on deep learning. Weather Forecast. 38, 467–486. https://doi.org/10.1175/WAF-D-22-0132.1.

Xie, J., Wang, Z., Yang, S., Liu, Y., Hu, Y., Guo, D., Shi, H., Liu, E., 2026. Quasi-biweekly oscillation of the Tibetan Plateau surface forcing during summer: spatio-temporal propagation and impact monitoring. J. Clim. 1. https://doi.org/10.1175/JCLI-D-25-0660.1.

Yan, Y., Liu, B., Zhu, C., 2025. Constraining subseasonal forecast skill for spring 2024 extreme rainfall in south China by extratropical atmospheric initial conditions. J. Geophys. Res. Atmos. 130, e2025JD043738. https://doi.org/10.1029/2025JD043738.

Yanai, M., 1961. A detailed analysis of typhoon formation. J. Meteorol. Soc. Jpn. Ser. II 39, 187–214. https://doi.org/10.2151/jmsj1923.39.4_187.

Yang, J., Bao, Q., Wang, B., He, H., Gao, M., Gong, D., 2017. Characterizing two types of transient intraseasonal oscillations in the Eastern Tibetan Plateau summer rainfall. Clim. Dyn. 48. https://doi.org/10.1007/s00382-016-3170-z.

Yang, J., Wang, B., Wang, B., Bao, Q., 2010. Biweekly and 21–30-day variations of the subtropical summer monsoon rainfall over the lower reach of the Yangtze River Basin. J. Clim. 23, 1146–1159. https://doi.org/10.1175/2009JCLI3005.1.

Yang, M., Shi, X., Yuan, C., Lu, X., Liu, J., 2023. Summer extreme precipitation in southern China from the perspective of moisture static energy. J. Clim. 36, 4967–4986. https://doi.org/10.1175/JCLI-D-22-0627.1.

Yu, W., Liu, Y., Xu, L., Wu, G., Yang, S., Chen, D., Yang, X., Hu, C., He, B., 2022. Potential impact of spring thermal forcing over the Tibetan Plateau on the following winter El Niño–Southern Oscillation. Geophys. Res. Lett. 49, e2021GL097234. https://doi.org/10.1029/2021GL097234.

Yu, W., Wang, D., Deng, K., Liu, Y., Chen, D., Lin, S., Peng, Y., 2025. Impacts of North Atlantic tripole SSTAs mode and its three individual components on ENSO. NPJ Clim. Atmos. Sci. 8, 373. https://doi.org/10.1038/s41612-025-01249-9.

Yuan, Y., Hsu, P.-C., Li, W., 2023. Characteristics and dynamics of two distinct quasi-biweekly oscillations in the Tibetan Plateau summer monsoon. Clim. Dyn. 61, 91–109. https://doi.org/10.1007/s00382-022-06575-9.

Zang, Y., Hsu, P.-C., Gao, Y., 2024. The impacts of 10—20 d vs. 30—60 d low-frequency oscillations on South China pre-flood season persistent heavy rainfall: comparison and associated mechanisms. Acta Meteor. Sin. 82, 137–154. https://doi.org/10.11676/qxxb2024.20230033.

Zeng, Z., Sun, J., 2023. Interannual variations in the intraseasonal variability of spring precipitation over southern China and the possible mechanisms. J. Clim. 36, 5319–5336. https://doi.org/10.1175/JCLI-D-22-0863.1.

Zhang, H., Ren, H.-L., Zhou, F., 2024. Understanding the dominant intraseasonal modes of the springtime primary diabatic heating over the eastern Tibetan Plateau. Clim. Dyn. 62, 9489–9504. https://doi.org/10.1007/s00382-024-07407-8.

Zhu, Z., Wang, M., Wang, J., Duan, A., Liu, B., Yu, Z., 2025. Intraseasonal oscillation intensity variations of the atmospheric heat source over the Tibetan Plateau and their relationship with summer precipitation. J. Clim. 38, 931–946. https://doi.org/10.1175/JCLI-D-24-0216.1.

Zhu, Z., Wang, M., Wang, J., Duan, A., Zhou, S., Yu, Z., 2026. Interannual co-variability of Tibetan Plateau Quasi-Biweekly oscillation intensity and asymmetric summer precipitation in China. Atmos. Res. 336, 108898. https://doi.org/10.1016/j.atmosres.2026.108898.